Ocean Engineering 339 (2025) 122118

Contents lists available at ScienceDirect

Ocean Engineering

journal homepage: www.elsevier.com/locate/oceaneng

Research paper

Multidimensional numerical analysis of wedge-shaped bow wave breaking: Statistical signatures, critical frequencies, and energy distribution

Xinyi Li [a], Bowei Song [b], Jianhua Wang [a,*], Decheng Wan [a], Jian Xu [c]

[a] Computational Marine Hydrodynamics Lab (CMHL), School of Ocean and Civil Engineering, Shanghai Jiao Tong University, Shanghai, 200240, China
[b] Ningbo Pilot Station, Ningbo Dagang Pilotage Co., Ltd., Ningbo, 315020, China
[c] China Shipbuilding Ninth Design & Research Institute Engineering Co., Ltd., Shanghai, 200063, China

ARTICLE INFO

Keywords:
Bow wave breaking
Wedge-shaped bow
Statistical characteristics analysis
Frequency analysis

ABSTRACT

This study investigates bow wave breaking dynamics using OpenFOAM. A simplified 3D wedge geometry is employed to examine half-angle effects. This study divides the bow wave surface into two perspectives, Top View and Bottom View, to distinguish different bow wave breaking phenomena. The impact of half angle variations is quantified through three distinct analytical dimensions: statistical characterization of bow wave distribution and oscillation amplitudes, demarcation of dominant frequency bands corresponding to specific wave breaking phenomena, spatial energy distribution mapping bow wave breaking. Results demonstrate that increasing the half angle of wedge-shaped bow significantly intensifies wave breaking, with enhanced surface tearing, jetting, and splashing. The bow wave zone exhibits notable spatial expansion along with increased wave heights and amplified oscillation amplitudes as the half angle increases. The bow wave spreading angle is found to be approximately 1.86 times the half angle. These changes correspond to greater surface turbulence and induce higher frequency components in wave fluctuations, leading to an upward shift in dominant frequency ranges. Notably, jetting, splashing, and underwater air tube behaviors are characterized by key frequency bands in the 20–60 Hz range. Furthermore, the spatial energy distribution shows strong correlation with plunging, while larger half-angles promote more intense energy dissipation along the axial direction. This work provides fundamental flow field data and quantitative analysis methods for advancing the understanding of bow wave breaking dynamics.

1. Introduction

During wave breaking, different frequency components interact, causing energy transfer. As the wave crest becomes steeper, wave breaking occurs when the steepness exceeds a certain threshold(Liu, 2018). Bow wave breaking is a type of wave breaking that occurs at the bow when the ship is at medium to high speeds. It can primarily be classified into plunging breaking and spilling breaking. Plunging breaking is observed in fast ships with sharp bows, while spilling occurs in vessels with broader hulls (Deike et al., 2015). The plunging, spray formation, and air entrainment in bow wave breaking are key contributors to underwater radiated noise and white wakes. Studying bow wave breaking is vital for military vessels, the noise can reveal the vessel's location, thus compromising its stealth capabilities and tactical performance. Furthermore, wave breaking causes significant energy dissipation, leading to increased resistance and higher fuel consumption. Therefore, research on bow wave breaking is essential for enhancing stealth, optimizing wave-breaking resistance, and reducing fuel use. These studies provide critical theoretical frameworks and predictive tools for eco-friendly hull design, supporting the maritime industry's transition toward carbon-neutral operations.

Bow wave breaking exhibits multi-scale characteristics. At the small scale, splashing and air entrainment are much smaller than the ship length. At the large scale, the bow wave includes induced vortices and free surface scars. Analyzing small-scale flow and its impact on large-scale characteristics is a crucial topic(Deike et al., 2015). To study this phenomenon, model test is one of the main approaches. Baba(Baba, 1969) combined experimental and theoretical research to show that bow wave breaking increases viscous resistance. It was found that the turbulent energy dissipation from wave breaking is closely related to the additional resistance. Miyata and Inui(Miyata and Inui, 1984) employed pitot tubes and wave height gauges to investigate the wave profiles of

* Corresponding author.
E-mail address: jianhuawang@sjtu.edu.cn (J. Wang).

https://doi.org/10.1016/j.oceaneng.2025.122118
Received 13 May 2025; Received in revised form 25 June 2025; Accepted 3 July 2025
Available online 9 July 2025

spilling bow wave breaking and the variations in the velocity field around the ship. Olivieri et al. (2003)˙ (Olivieri et al., 2007) measured the velocity field beneath the free surface and wave heights using a five-hole pitot tube and wave gauges. Dong et al. (1997) used Particle Image Velocimetry (PIV) technology to observe the bow wave profiles of the DTMB 5512 ship model at Froude numbers Fr = 0.28 and Fr = 0.45. They analyzed the local velocity and vorticity fields in the bow wave region, finding a strong correlation between bow wave evolution and vorticity. Roth et al. (1999) used PIV technology to study the bow wave evolution on a DDG-51 ship model. Their research indicated that turbulence forms at the wave crest, leading to significant changes in the velocity field. Liu et al. (2022). conducted model tests on the KCS ship, providing experimental data for the KCS bow wave breaking.

With advancements in CFD technology, numerical simulations have been used to study bow wave breaking, analyzing factors like speed, scale, and ship attitude. Wang et al. (2020) simulated the bow wave breaking phenomenon of the KCS ship model at Fr = 0.35 and Fr = 0.40. The study showed that as sailing speed increases, the air entrainment phenomenon becomes more pronounced, and the breaking area extends. Ren et al. (2018) using the KCS ship model, analyzed the effect of sailing speed on the bow wave breaking. The study found that at Fr = 0.35, the first plunging event of the KCS model would create cavity, which results in air entrainment. Mao et al. (2024) analyzed the spatio-temporal characteristics of the cavity at different sailing speeds. Xie et al. (2021) conducted a study on the scale effects of KCS bow wave breaking at different scales. The results indicated that, as the scale increased, the third and fourth plunging events could be maintained. Wang et al. (2023) analyzed the flow field results of the KCS bow wave at three different scales, covering bow wave profiles and vorticity at various cross-sections. Li et al. (2024) studied the statistical and spectral characteristics of the KCS bow wave breaking at different trim angles.

Although research on standard ship hulls is well-established, most studies cannot fully explain the influence of geometric factors on bow wave breaking. To address this, some studies simplify the bow shape to basic geometries, such as wedge-shaped bows and slanted flat plates, which help isolate the impact of geometric features. Waniewski et al. (2002) used high-speed cameras to observe the dynamics and air entrainment process of a simplified wedge-shaped bow. The results showed that the bow wave height exhibited nonlinear behavior, and the bow wave surface disturbances might be generated by gravity waves, forming plunging jets that eventually break into a string of droplets and trigger bubble clouds (Waniewski, 1999)˙ (Waniewski et al., 2001). Noblesse et al. (2008) also conducted bow wave experiments using a slanted flat plate. Based on the experimental observations, they summarized theoretical formulas defining the bow wave height, the distance between the ship's bow and the wave crest, and the wave shape. Delhommeau et al. (2009) studied the effect of yaw angles on the bow wave by towing a rectangular flat plate at nine different yaw angles. Their results showed that yaw angles significantly enhanced the instability of the bow wave. Wang et al. (2025) simplified the ship's bow as a wedge-shaped structure. This experiment comprehensively considered influencing factors such as flow velocity, draft, half angle, flare angle, and yaw angle, studying the sensitivity of bow wave breaking to these factors. Wang et al. (2010) and Koo et al. (Koo and Kang, 2021) performed numerical simulations on the bow wave breaking of a wedge-shaped geometry under Fr = 2.93,studying wave profile, plunging jet and air entrainment. Hu et al. (2021) simulated the flow structure and bubble entrainment phenomenon of a rectangular plate bow wave breaking.

Most existing studies on the influence of geometric factors on bow wave breaking are qualitative or involve only basic quantitative analysis. And few studies examine this phenomenon from the perspectives of frequency or energy. This paper simplifies the ship bow into a wedge-shaped geometry and investigates the influence of the half-angle, as a key geometric parameter, on bow wave breaking phenomena. First, from a qualitative perspective, the formation and evolution of bow wave profiles under different half-angles are analyzed through the velocity fields and vortex structures of bow waves. Subsequently, bow wave breaking under various half-angles is quantitatively analyzed from three perspectives: statistical, frequency-domain, and energy-based methods. The statistical approach quantified the time-averaged distribution and oscillatory intensity of the bow wave. The frequency-domain analysis identified the power spectral density (PSD) characteristics of specific bow wave breaking events and their dominant frequency ranges. Meanwhile, the energy-based method revealed correlations between energy distribution and the evolutionary process of bow wave breaking. This study introduces an integrated quantitative-qualitative analytical framework, with the aim of providing a potential methodological starting point for related research.

2. Numerical approach

2.1. Numerical methodology

In this study, the fluid is treated as incompressible, and the air-water interface is captured using the Volume of Fluid (VOF) method, specifically the PLIC method(Youngs, 1982). In this approach, the interface within each cell is approximated as a plane perpendicular to the normal direction of the interface. VOF method introduces a volume fraction α to describe the interface. $\alpha = 1$ represents water and $\alpha = 0$ represents air, and an interface exists when α lies between 0 and 1.

By incorporating the convection equation of α, the incompressible Navier-Stokes equations with the interface are obtained.

$$\nabla \cdot \mathbf{U} = 0 \tag{1}$$

$$\frac{\partial \rho \mathbf{U}}{\partial t} + \nabla \cdot (\rho \mathbf{U}\mathbf{U}) = \nabla \cdot \tau - \nabla p + \rho \mathbf{g} + \mathbf{F} \tag{2}$$

$$\frac{\partial \alpha}{\partial t} + \mathbf{U} \cdot \nabla \alpha = 0 \tag{3}$$

In which, ρ is the fluid's mixed density, $\mathbf{U}$ is the velocity, and p is the pressure. $\nabla \cdot \tau$、 ∇p、 $\rho \mathbf{g}$ and $\mathbf{F}$ represent the viscous force, pressure force, gravitational force, and surface tension respectively.

The turbulence model used in this study is the DDES model, which bridges the RANS and LES models. The RANS model is applied near the wall, while the LES model is used in the far-field region to capture vortices. The RANS model is based on $k - \omega SST$ (Menter, 1994):

$$\frac{\partial k}{\partial t} + \nabla \cdot (\mathbf{U}k) = \widetilde{G} - \beta^* k\omega + \nabla \cdot [(\nu + \alpha_k \nu_t)\nabla k] \tag{4}$$

$$\frac{\partial \omega}{\partial t} + \nabla \cdot (\mathbf{U}\omega) = \gamma S^2 - \beta^* \omega^2 + \nabla \cdot [(\nu + \alpha_\omega \nu_t)\nabla \omega] + (1 - F_1) CD_{k\omega} \tag{5}$$

Where k represents the turbulent kinetic energy and ω is the vorticity. ν is the kinematic viscosity and ν_t is the turbulent viscosity. F_1 is the blending function and $CD_{k\omega}$ is defined as follows:

$$F_1 = \tan h\left(\left\{\min\left[\max\left(\frac{\sqrt{k}}{\beta^* ky}, \frac{500\nu}{y^2 w}\right), \frac{4\alpha_{\omega 2} k}{CD^*_{k\omega}}\right]\right\}\right) \tag{6}$$

$$CD^*_{k\omega} = \max\left(CD_{k\omega}, 10^{-10}\right) \tag{7}$$

Then the source term $\widetilde{G}$ and mean strain rate coefficient S are defined as follows:

$$\widetilde{G} = \min(G, 10\beta^* k\omega) \tag{8}$$

$$S = \sqrt{2S_{ij}S_{ji}} \tag{9}$$

$$G = \nu_t S^2 \tag{10}$$

$$S_{ij} = \frac{1}{2}\left(\nabla \mathbf{U} + \nabla \mathbf{U}^{\mathrm{T}}\right) \tag{11}$$

Besides these, γ, β^*, α_k and α_ω involved in eq. (4) and eq. (5) are constants.

The DDES model(Spalart et al., 2006) is an enhanced turbulence model derived from the DES model (Strelets, 2001). The DES model bridges the RANS and LES models through a blending function. The DDES model introduces a delay function to address the issue of premature activation of the LES model in the DES approach. The blending function calculates the local turbulence characteristic length L_{DES} and determines whether to switch between the RANS and LES models based on it.

$$L_{DES} = \min(L_{RANS}, L_{LES}) \tag{12}$$

$$L_{RANS} = \sqrt{k} \Big/ (C_\mu \omega) \tag{13}$$

$$L_{LES} = C_{DES}\Delta \tag{14}$$

In which C_μ and C_{DES} is the model parameters, and Δ is the grid size. This indicates that the activation of the LES model is determined by the grid size. As a result, the LES model is effectively turned off in the near-wall region. However, relying solely on this criterion may lead to the premature activation of the LES model, which in turn could result in flow separation. Therefore, the delay function f_d and the delay factor r_d are introduced:

$$f_d = 1 - \tanh\left(512 r_d^3\right) \tag{15}$$

$$r_d = \frac{\nu_t + \nu}{\sqrt{u_{ij}u_{ji}}\kappa^2 d^2} \tag{16}$$

In the above equation, d is the distance to the wall. After introducing f_d, the characteristic length of the DDES model L_{DDES} can be described as follows:

$$L_{DDES} = L_{RANS} - f_d \max(0, L_{RANS} - L_{LES}) \tag{17}$$

Considering the importance and the unsteadiness of small-scale structures in complicated bow wave breaking phenomenon, this study selects the high-precision geometric VOF method PLIC and the high-precision turbulence model DDES to meet the detailed requirements.

2.2. Data processing method

The data analysis methods in this paper mainly include the bow wave height extraction, its statistical and frequency analysis and energy calculation.

The bow wave height extraction method involves extracting the height of the air-water interface. The interface is defined as the isosurface where $\alpha = 0.5$. However, due to the air entrainment caused by plunging breaking, multiple air-water interfaces can appear at the same location. The built-in wave height detection tool in OpenFOAM cannot distinguish these interfaces, which makes it difficult to distinguish between different wave breaking phenomena. To address this problem, specific post-processing are performed based on the stored interface data. Then the wave height can then be interpreted from both the Top View and Bottom View, as shown in Fig. 1. In locations with a single interface, both the Top and Bottom views are marked in black to indicate consistency. In regions with multiple interfaces, the Top View is marked in red to represent the top surface, while the Bottom View is marked in blue to represent the bottom surface. This distinction enables the identification of additional wave-breaking features, such as splashing, jetting, cavity formation, and air tube.

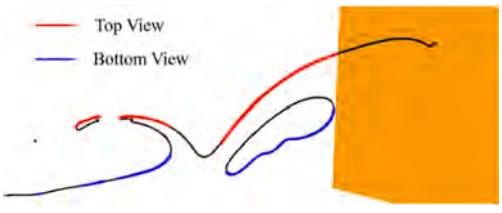

Fig. 1. Definition of top view and bottom view.

The statistical analysis method involves recording wave height data from each temporal snapshot and applying the previously described extraction method to differentiate between the Top View and Bottom View. Subsequently, the mean z_{Mean} and standard deviation z_{SD} of the bow wave height are computed for both views based on these snapshots.

$$z_{Mean} = \frac{\sum_{i=1}^{n}(z_i/L_1)}{n} \tag{18}$$

$$z_{SD} = \sqrt{\frac{\sum_{i=1}^{n}(z_i/L_1 - z_{Mean})^2}{n}} \tag{19}$$

In the equations above, n denotes the number of samples, z_i represents the instantaneous wave height, and L_1 is the side length of the wedge. In this study, $n = 10{,}000$, equivalent to a total duration of 50 s with a sampling interval of 0.005 s between consecutive snapshots.

The frequency-domain analysis of wave height is performed using Fourier transform and Fourier modes. The sampling frequency is set to 200 Hz with 10,000 data points, and a Hanning window is applied for spectral analysis. Following Sun et al. (2020), Fourier modes are employed to characterize the spatial distribution of PSD amplitude at each frequency, which effectively represents the energy spatial distribution across the frequency spectrum. Building upon their work, this study introduces modified definitions using PSD amplitude to establish the normalized dimensionless PSD $E_\eta^*(f)$ and energy ratio of the bow wave height σ_h within selected frequency ranges as follows:

$$E_\eta^*(f) = A_f \Big/ \sum_{i=0}^{\infty} A_i \tag{20}$$

$$\sigma_h = \sum_{i=f_{LB}}^{f_{UB}} E_\eta^*(i) \tag{21}$$

Here, A_f is the PSD amplitude at frequency f, while A_i denotes the PSD amplitude at discrete frequencies within the selected range (f_{LB}, f_{UB}], where i indexes each frequency component within the range, f_{LB} and f_{UB} correspond to the lower and upper bounds of the frequency range, respectively.

The mechanical energy E_M is calculated as the sum of kinetic energy E_K and potential energy E_P.

$$E_M = E_K + E_P \tag{22}$$

The kinetic energy component E_K and potential energy component E_P can be calculated as follows:

$$E_K = \frac{1}{2}\int_{d\le 0} \rho\left[(u-U)^2 + v^2 + w^2\right] dxdy \tag{23}$$

$$E_P = \frac{1}{2}\int_{d\le 0} \rho y dxdy \tag{24}$$

In which $d \le 0$ represents the underwater region, where the integration is performed over a specified cross-section. E_K is defined with the inflow velocity U removed, isolating the energy contribution induced by the wedge-shaped bow. The scaling factor $\rho_w g\lambda^3$ is used to non-dimensionalize the energy terms, resulting in normalized terms E_K^*, E_P^* and E_M^*. λ represents the projected wavelength of the divergent wave in the transverse direction, serving as the characteristic length scale of the

lateral propagation of bow wave plunging. It is estimated based on the simulated transverse wavelength and the divergent angle. The kinetic energy ratio σ_K, defined as the proportion of kinetic energy to total mechanical energy, is given by:

$$\sigma_K = \frac{E_K^*}{E_M^*} \tag{25}$$

The third-generation vortex identification technique Ω_R (Liu et al., 2019) is used to capture the vortex structures around the wedge-shaped bows. Omega-Liutex (Ω_R) method was recently proposed by combining the Omega and Liutex/Rortex approaches. Ω_R is defined as:

$$\Omega_R = \frac{\beta^2}{\alpha^2 + \beta^2 + \varepsilon} \tag{26}$$

where ε is a small positive parameter introduced to suppress numerical noise. It is empirically set as:

$$\varepsilon = b \times \max(\beta^2 - \alpha^2) \tag{27}$$

with b = 0.001 typically. This avoids manual tuning and ensures stability.

And in equation (26) α and β are defined as:

$$\alpha = \frac{1}{2}\sqrt{\left(\frac{\partial V}{\partial Y} - \frac{\partial U}{\partial X}\right)^2 + \left(\frac{\partial V}{\partial X} - \frac{\partial U}{\partial Y}\right)^2} \tag{28}$$

$$\beta = \frac{1}{2}\left(\frac{\partial V}{\partial X} - \frac{\partial U}{\partial Y}\right) \tag{29}$$

Here, U, V, W represent the velocity components in the XYZ coordinate system.

The iso-surface is recommended at $\Omega_R = 0.52$ for visualizing vortices, for flows with excessive small-scale or noisy vortices, a slightly higher threshold may be used for better clarity.

3. Numerical setup

3.1. Geometry and numerical parameters

The simplified wedge-shaped bow selected in this study is depicted in Fig. 2. The geometric parameters of the wedge-shaped bow mainly include the height H, the draught d, the side length L_1 and the half angle θ.

The half-angle θ is adopted as the primary variable to systematically examine its influence on bow wave breaking phenomena. All other geometric parameters and inflow conditions remain constant, with parameters detailed in Table 1. The inflow velocity U is oriented along the positive x-axis as shown in Fig. 2. Three distinct half angles are selected for the study: 15°, 22.5°, and 30°. The corresponding wedge-shaped models are shown in Fig. 3. During the simulations, these models are fixed. The numerical parameters are based on the experiments by Wang et al. (2025), whose dataset is subsequently employed for validation and verification purposes.

Additionally, some physical constants involved in the simulations are set based on the experimental conditions of Wang et al. Since the water temperature in the experiments is 32 °C, the water density ρ_w is set to 996 kg/m^3, the kinematic viscosity of water ν_w is set to 0.803×10^{-6}m^2/s.

3.2. Computational domain and mesh

The computational domain is shown as Fig. 4. Considering the symmetry characteristics of the problem, only a half wedge is modeled

Table 1
Main numerical parameters.

Condition parameters	Value
Flow velocity U	2.5 (m/s)
Height H	0.5 (m)
Draught d	0.075 (m)
Chord length L_1	0.75 (m)
half angle θ	15,22.5,30 (°)

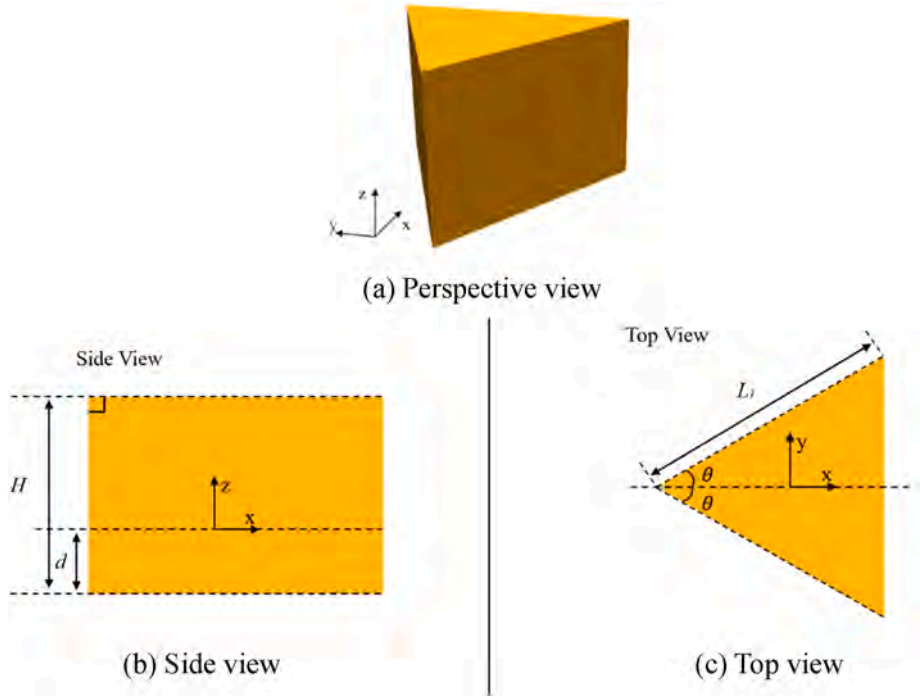

Fig. 2. Simplified wedge-shaped bow.

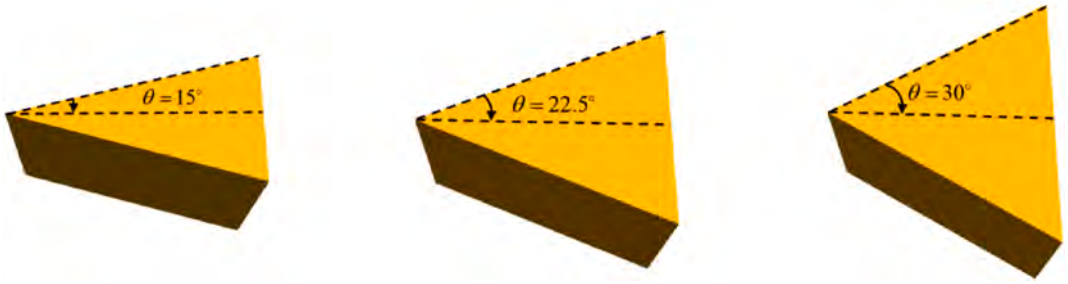

Fig. 3. Wedge-shaped bow with different half angles.

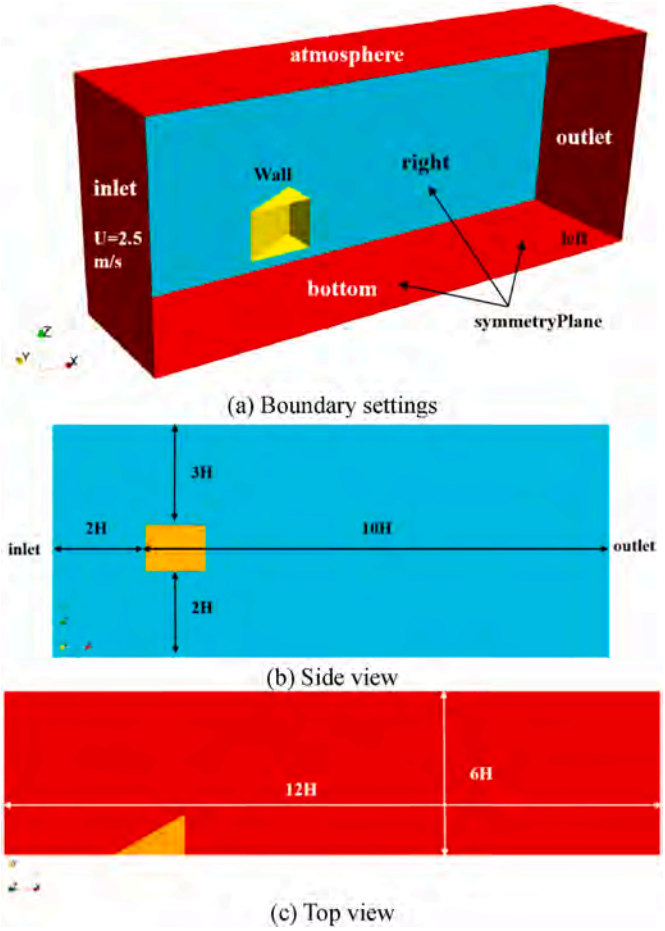

Fig. 4. Computational domain settings.

to optimize computational efficiency. The origin of the computational domain is located at intersection of the waterline and the wedge's leading edge. The positive X-axis is directed from the tip of the wedge towards its trailing end. The positive Z-axis is directed vertically upward and the positive Y-axis follows the right-hand coordinate system convention.

Fig. 4 (a) shows the boundary conditions of the entire domain. The 'inlet' is set as the velocity inlet boundary with $U = 2.5\ m/\ s$. The 'atmosphere' is the top boundary, which combines both pressure outlet and velocity outlet characteristics. The 'outlet' is the multi-phase flow velocity outlet boundary. The left and right side boundaries, and the 'bottom', are set as symmetry boundaries. The wedge-shaped bow itself is set as a no-slip wall. The computational domain measures 12H in length and 6H in width. The distances between the wedge and each boundary are shown in Fig. 4(b) and (c).

The computational mesh is progressively refined from the far-field to the near-field. With each refinement level, the grid length in each direction is reduced by half compared to the previous level. Since the refinement method is similar for different half angles, only the mesh for the 30° half angle is shown in Fig. 5 as an example. The refinement approach based on refinement levels is detailed in Fig. 6.

The main refined regions comprised three distinct zones: the area surrounding the wedge, the free surface region, and the wave region. The area surrounding the wedge is refined with 3 levels, fully enclosing the wedge-shaped bow. The free surface region, encompassing the full range of surface fluctuations, is similarly refined with 3 levels. The wave region is refined with 4 levels of grids, to resolve both bow wave dynamics and turbulent wake features, enabling capture of small-scale flow structures.

3.3. Grid convergence and validation study

Based on the experimental data, the wave breaking phenomenon is particularly intense when the half angle $\theta = 30°$, which makes the numerical simulation more difficult to converge. Therefore the case with $\theta = 30°$ is selected. Based on the above mesh refinement strategy, four different meshes are generated by adjusting the base mesh size as Table 2. The boundary layer growth rate is set to 1.2, and the y^+ is set to 60. The grid convergence is studied through resistance validation and wave profile analysis. The minimum mesh size refers to the smallest refined grid outside the boundary layer region.

The temporal evolution of resistance in Fig. 7 demonstrates consistent variation trends across all mesh configurations. As the mesh density increases, the oscillation amplitudes of the resistance curves progressively decrease. Furthermore, the resistance curves for Mesh 3 and Mesh 4 exhibit near-complete overlap, indicating that Mesh 3 (919w) satisfies the convergence criteria. Additionally, the grid convergence index (GCI) (Schwer, 2008) for resistance is calculated in Table 3 based on the results from Mesh 1, Mesh 2, and Mesh 3. The GCI values for all meshes are less than 5 %. This indicates asymptotic convergence behavior and excellent numerical convergence. Therefore, it can be concluded that the mesh has achieved good convergence.

Given the complex interfacial dynamics characteristic of bow wave breaking, an additional mesh convergence analysis was performed for wave profiles at cross-sections $x/L_1 = 0.6$ and $x/L_1 = 0.8$ as shown in Fig. 8. While Mesh 2 fails to resolve fine-scale features such as splashing, these phenomena are adequately captured by both Mesh 3 and Mesh 4. Also, the wave profiles captured by Mesh 3 show excellent agreement with those from Mesh 4. Therefore, it can be concluded that Mesh 3 provides sufficient resolution for accurate simulation of bow wave breaking.

The Mesh 3 refinement strategy is applied to cases with different half angles, wherein the refinement region adjusted according to the bow wave height. Therefore, the mesh counts are 8.95 million at $\theta = 15°$, 9.07 million at $\theta = 22.5°$, and 9.19 million at $\theta = 30°$. The resistance at each half angle and the relative errors compared to the experimental data are all within 5 % as shown in Table 4, indicating that the simulations are accurate.

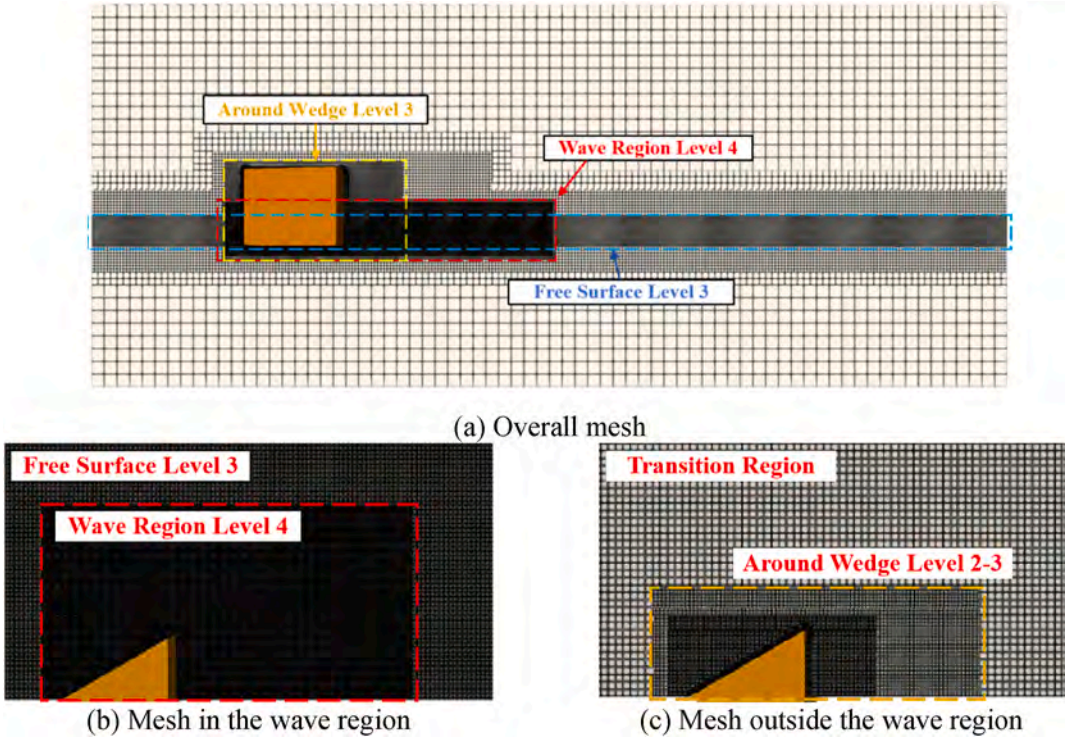

Fig. 5. Computational mesh settings.

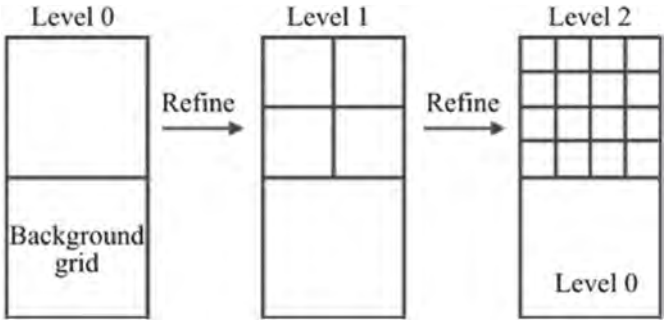

Fig. 6. Refinement level schematic diagram(Li et al., 2024).

Table 2
Mesh configurations.

Mesh	Base size (m)	Minimum size (m)	Total number (millions)
Mesh1	0.150	9.3×10^{-3}	2.32
Mesh2	0.107	6.7×10^{-3}	5.85
Mesh3	0.085	5.2×10^{-3}	9.19
Mesh4	0.078	4.9×10^{-3}	13.86

Finally, the entire bow wave structure is validated by comparing the simulation results with experimental photographs as shown in Fig. 9 to assess the accuracy of the numerical simulations. The results show that the bow wave heights and extents closely match the experimental measurements. The simulation successfully reproduces the overall bow wave shape, plunging, and surface scars. It also captures more pronounced jetting and splashing as the half angle increases, which align well with the experimental results. Although the current numerical method may not fully capture all the breaking details, it effectively reproduces key breaking features. Therefore, the simulation demonstrates high reliability in studying the bow wave breaking.

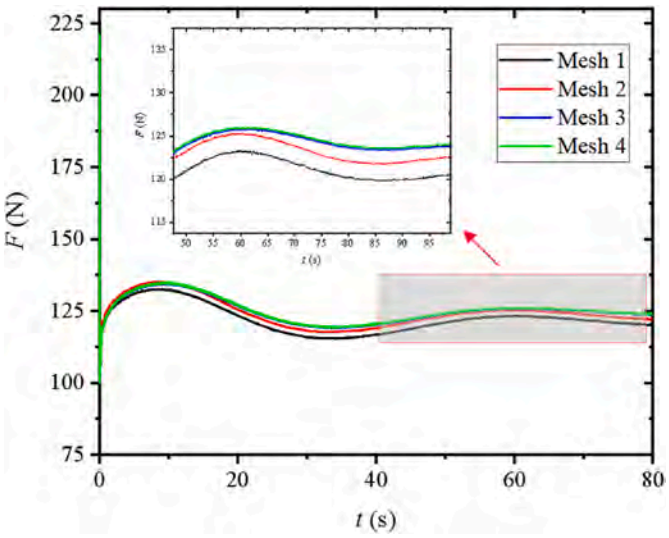

Fig. 7. Temporal evolution of resistance.

Table 3
Mesh convergence study.

Mesh	Refinement factor	Resistance (N)	Relative error between adjacent meshes (%)	GCI (%)
Mesh1	–	120.15	–	–
Mesh2	1.26	122.61	0.0201	3.415
Mesh3	1.4	123.77	0.0095	4.586

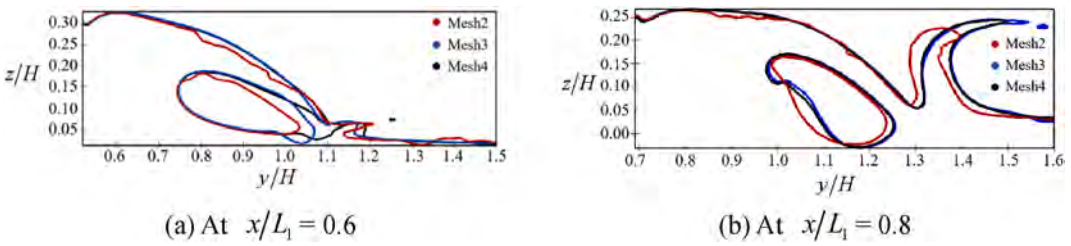

Fig. 8. Mesh convergence study of bow wave profiles.

Table 4
Comparison of experimental and numerical resistance.

Condition	CFD (N)	EFD (N)	Relative error (%)
$\theta =$ 15°	30.078	29.297	2.67
$\theta =$ 22.5°	65.658	63.913	2.73
$\theta =$ 30°	123.767	120.063	3.09

4. Results and discussion

4.1. Velocity field and vortex structure

The underwater velocity field around each wedge-shaped bow at a given moment is analyzed to examine the effect of half angle on the bow wave velocity distribution. Given the variations in the position and extent of the bow wave's plunging at different half angles, in this study, the sections where the first cavity forms and where the second plunging occurs are selected for velocity field comparison. The underwater velocity is non-dimensionalized by dividing the inflow velocity U (2.5 m/s). The axial, transverse and vertical velocities under the breaking free surface are shown as Fig. 10 Fig. 11 and Fig. 12.

The axial velocity indicates that, as the distance from the hull increases, the velocity gradually returns to the initial velocity. As the half angle increases, the distribution of low axial velocity becomes wider in both depth and width. This phenomenon directly results in the occurrence of the plunging at a more forward position as the half angle increases.

The transverse velocity primarily determines the extent of the bow wave region, while the vertical velocity governs the occurrence of the plunging. When the vertical velocity is insufficient and the transverse velocity is relatively large, spilling wave breaking is more likely to occur. Conversely, when the vertical velocity is sufficiently large, a jet is formed and strikes the free surface, leading to plunging wave breaking. As the half angle increases, the displacement effect on the fluid becomes more pronounced. The transverse velocity and the vertical velocities at locations such as cavities and water tongues, increases in magnitude. This results in a larger height and broader extent of the bow wave, with more pronounced air entrainment. Additionally, a larger half angle leads to a greater negative vertical velocity during the first plunging event, making subsequent plunging bow wave breaking more likely than spilling bow wave breaking. For instance, at $\theta =$ 15°, the second plunging event is close to a spilling wave, while at $\theta =$ 30°, the second plunging event is still a distinct plunging wave.

The vortex structures are extracted by selecting the isosurface of $\Omega_R = 0.65$. Fig. 13 shows the vortex distribution at $\theta = 30°$ as an example. It is observed that vortices are primarily distributed at the wave elevation and the areas where plunging, jetting, and splashing occur. The vortices induced by shear from surface elevation are generally opposite in rotation to those generated by internal shear due to the pulling effect at the wave toe during plunging. The presence of these vortices amplifies disturbances in the shear layers, potentially leading to vortex separation and shedding, which can trigger wave breaking. Positive-negative vortex pairs are mainly observed near the air tubes and bubbles. Positive–negative vortex pairs likely form as oppositely signed vortices, generated by stretching-induced shear, merge near the surface undulation interface. Inward crest overturning in this region further enhances vortex generation and interaction. Air tubes and bubbles tend to form here and exhibit repeated breakup and oscillation under the influence of

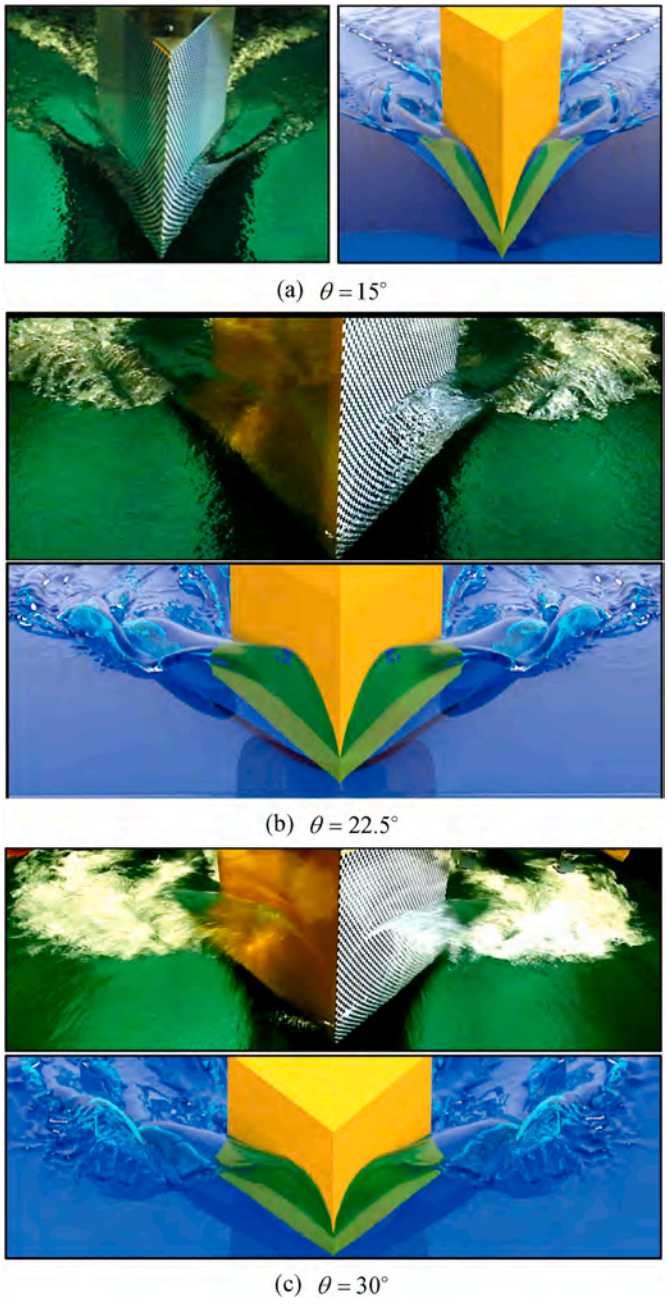

Fig. 9. Comparison of experimental and numerical bow wave structures.

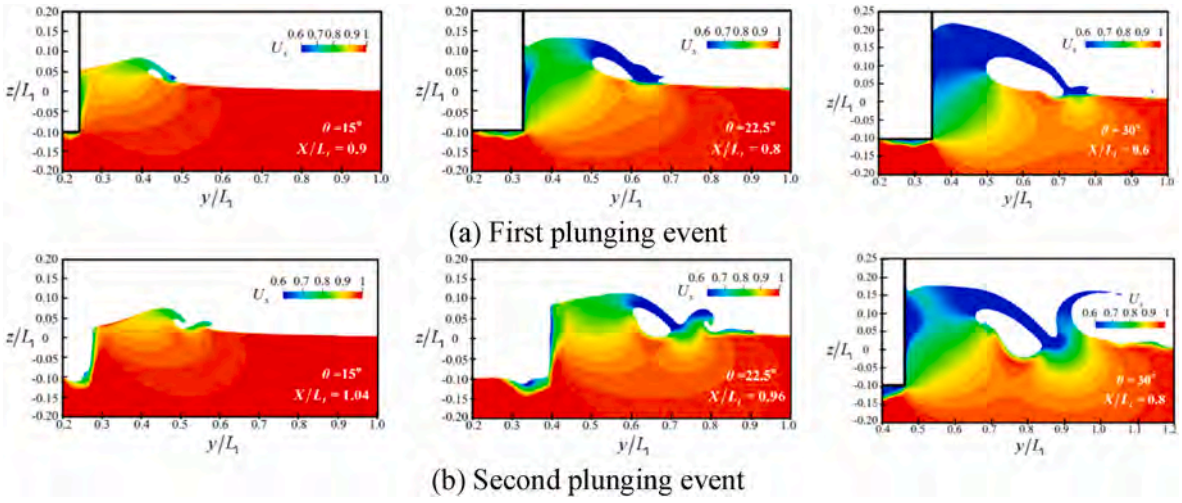

Fig. 10. Axial velocities under the breaking free surface.

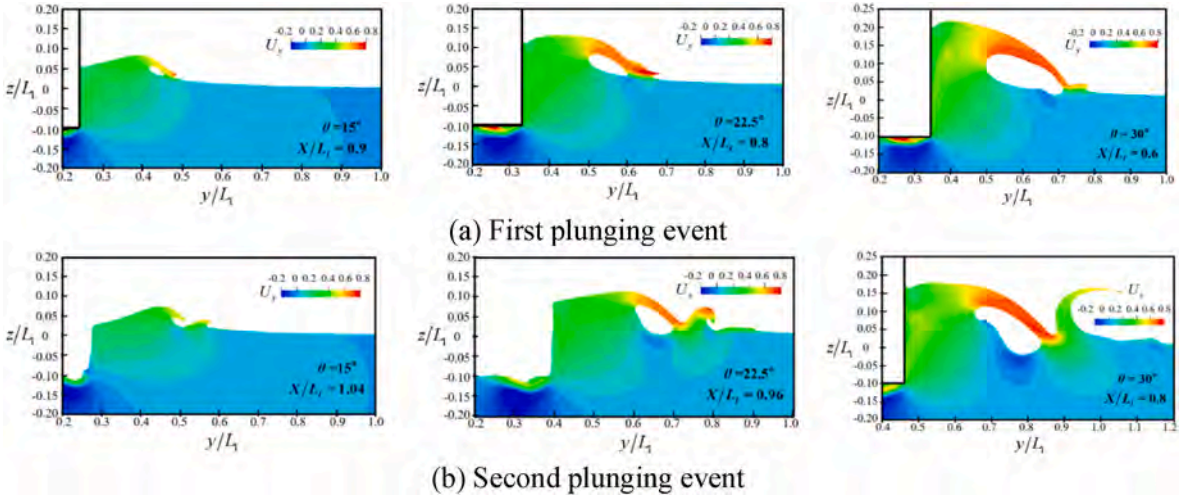

Fig. 11. Transverse velocities under the breaking free surface.

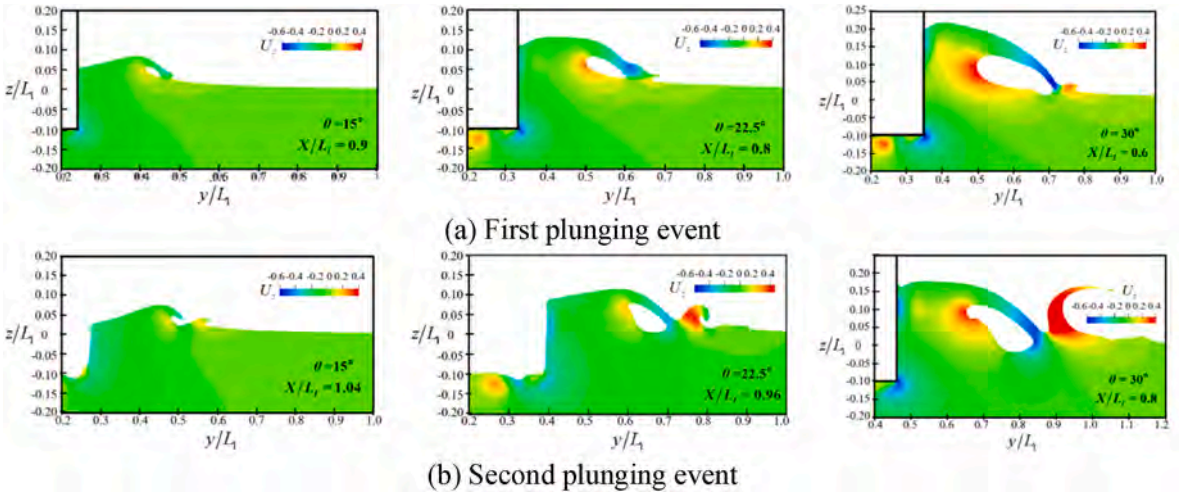

Fig. 12. Vertical velocities under the breaking free surface.

these vortices.

The effect of half angle on the vortex distribution in the bow wave area is investigated in Fig. 14. As the half angle increases, the vortex density around the wedge-shaped bow increases. Additionally, the number of breaking vortex significantly rises, especially in the bow wave plunging region. It can result in shear layer instability, vortex structure

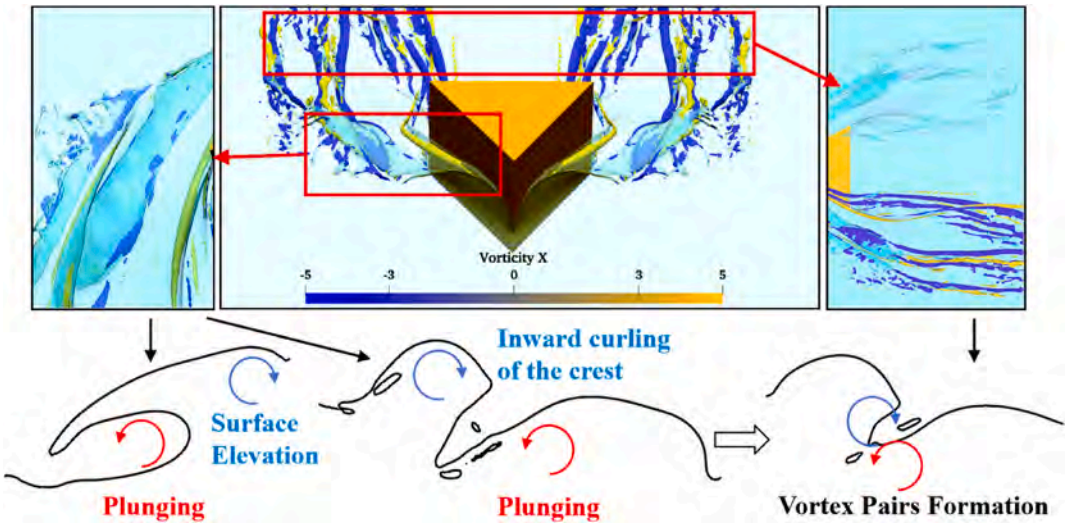

Fig. 13. Vortex distribution and local vortices.

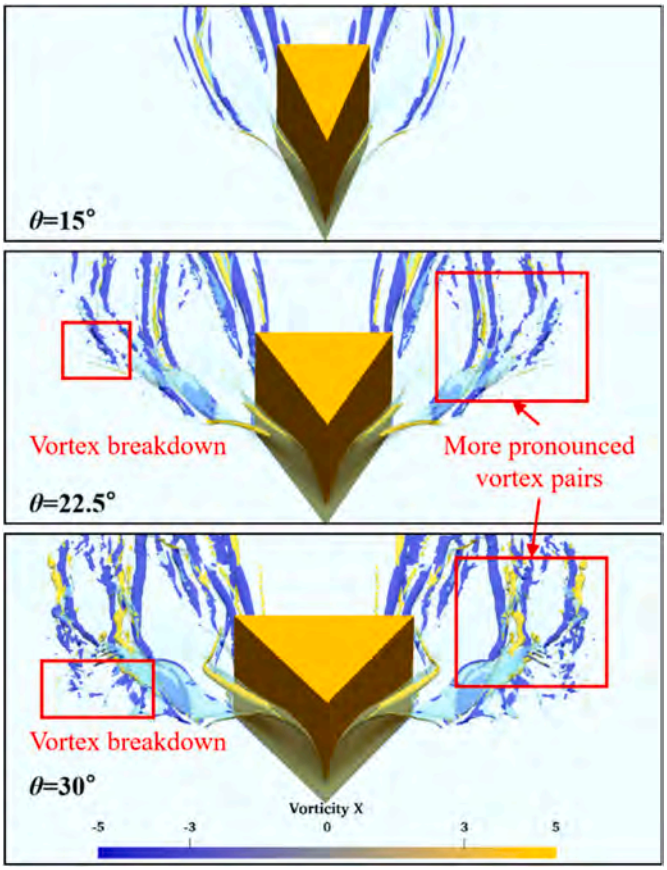

Fig. 14. Comparison of vortex structures at different half angles.

separation, and detachment phenomena, corresponding to an increase in jetting and splashing. These small-scale structures induce micro shear layers, further leading to more scattered vortices. Moreover, vortex pairs also increase significantly. As the half angle increases, the intensity of cavity formation becomes stronger, and vortex pairs further amplify the instability of free surface.

4.2. Statistical characteristics

This study initiates a quantitative investigation of bow wave breaking through statistical analysis. Two key parameters are calculated: the mean wave height z_{Mean} capturing the spatial distribution of wave elevation and the standard deviation z_{SD} quantifying temporal fluctuation intensity.

Fig. 15 presents the z_{Mean} distribution at each half angle. The Top View shows the spreading angle of the bow waves, while the Bottom View displays the size of the plunging region (the average width of cavity and jet). Individual plunging events are denoted as C_n, where n refers to the specific plunging number. The plunging events are identified based on the differences between the Top and Bottom views. At both $\theta = 15°$ and $\theta = 30°$, two plunging events occur, while at $\theta = 22.5°$, three plunging events are observed. This suggests that an increase in the half angle results in more energy in the water, leading to more plunging events. However, as the wave breaking becomes more intense and energy dissipation increases, the number of plunging events ultimately decreases. As the half angle increases, the bow wave height significantly rises. The width of the cavity increases significantly with the half angle. The air tubes are formed by the collapse of the cavities. At $\theta = 15°$and $\theta = 30°$ a single air tube is formed, while at $\theta = 22.5°$, the air tube splits into a bifurcated structure.

The bow wave spreading angle is determined through computer vision analysis of experimental photographs, utilizing a multi-view approach to enhance measurement accuracy. Fig. 16 illustrates the method, where R_n represents the reconstructed point on the wedge's bottom surface, and R_1M represents the spreading line. Perspective-induced errors are systematically reduced by performing statistical averaging across data obtained from multiple views.

Table 5 presents the bow wave spreading angles obtained from experimental measurements and numerical simulations across different half-angles. The comparative analysis reveals relative errors exceeding 5 % only at $\theta = 15°$. The absolute errors remain below 2.5° for all conditions, with the error being below 2°observed at $\theta = 15°$ and $\theta = 22.5°$. Given experimental uncertainties, the numerical results for the bow wave spreading angle are within a reasonable error range. Therefore, for half angles of 15°, 22.5°, and 30°, the bow wave spreading angles are 27.354 ± 2°, 39.542 ± 2°, and 55.183 ± 2.5°, respectively. Fig. 17 illustrates the linear relationship between spreading angles and half-angles, characterized by a growth rate coefficient $k = 1.86$. Conservatively adopting the maximum observed error of 2.5° as the uncertainty range, it can be concluded that the bow wave spreading angle induced by the wedge-shaped bow follows a pattern of 1.86 θ

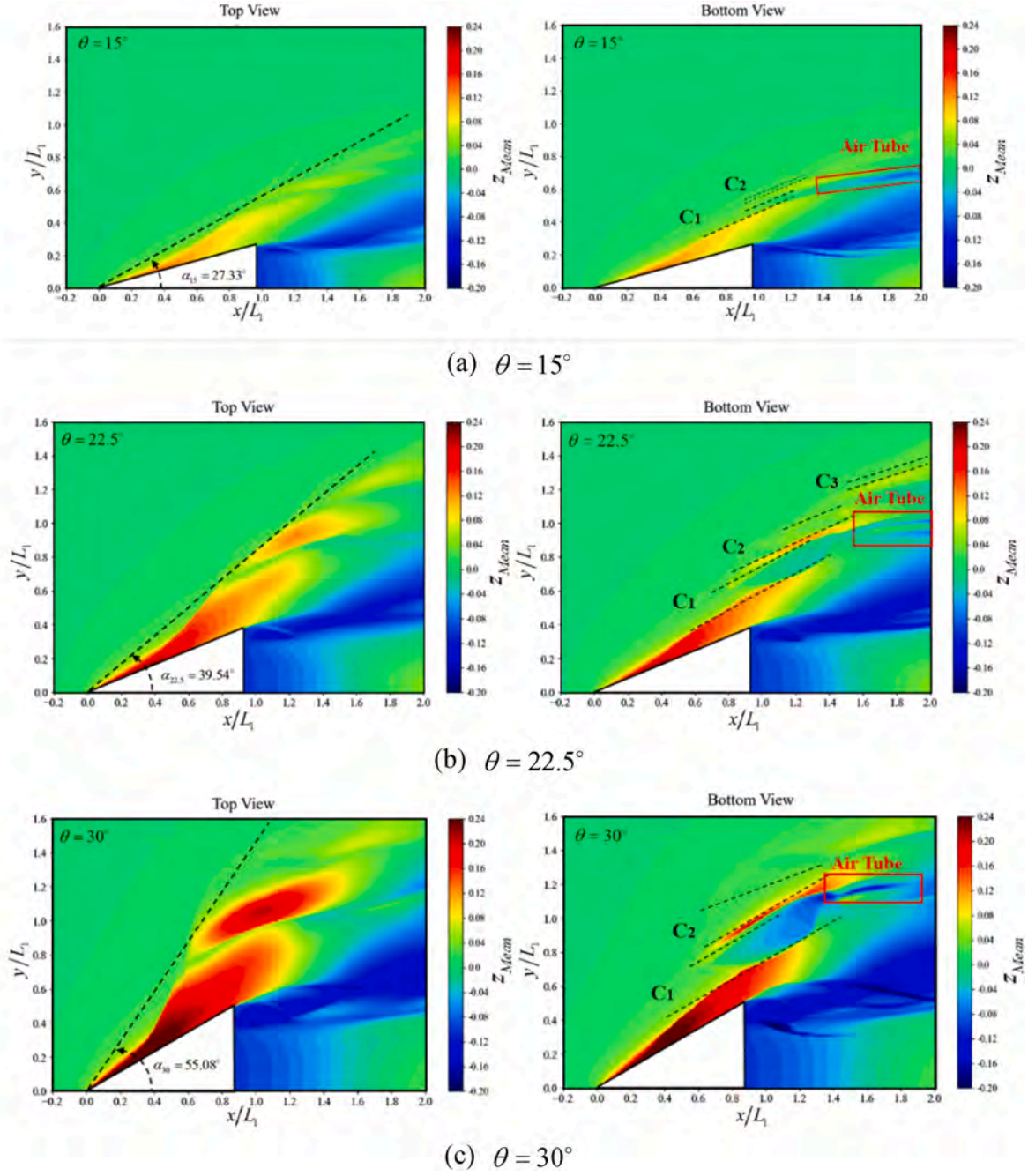

Fig. 15. Top and bottom views of z_{Mean}

±2.5°.

Fig. 18 presents the z_{SD} distribution for each condition. As the half angle increases, the amplitude and distribution range of the z_{SD} significantly increase, indicating more intense wave fluctuations and a wider fluctuation range.

High z_{SD} in the Top View are mainly distributed around the edges of the first plunging event, the second (or third) plunging regions, and the outer spilling wave breaking area. In other areas, z_{SD} tends to zero, which can be considered quasi-steady flow. Therefore, the initial plunging event can be seen as a quasi-steady flow, with potential fluctuations and local breaking phenomena at the edges. The local breaking are more pronounced at $\theta = 22.5°$. At the second plunging location, intense wave breaking occurs for all conditions. The significant increase in z_{SD} indicates the intense fluctuations caused by wave breaking. The z_{SD} peak lines are located further outward compared to the z_{Mean} peak line, indicating the potential energy accumulated at the wave crest is converted into the energy required for wave breaking as the water tongue moves outward. Specifically, the third plunging at $\theta = 22.5°$ shows a relative high z_{SD} both before and after the plunging, indicating that this third event is an unsteady phenomenon. In the Bottom View, high z_{SD} are mainly distributed in the air tube region. It is evident that the high z_{SD} range in air tube area exceeds the z_{Mean} range, indicating that the air tube occasionally undergoes lateral oscillations and repeated growth and collapse.

To further quantify the wave height and oscillation intensity of bow waves, a comparative analysis of z_{Mean} and z_{SD} was conducted on several X-direction cross-sections from both Top and Bottom Views as shown in Fig. 19. Given the distinct bow wave distribution patterns across different half-angles, the selected cross-sections correspond to the mid-

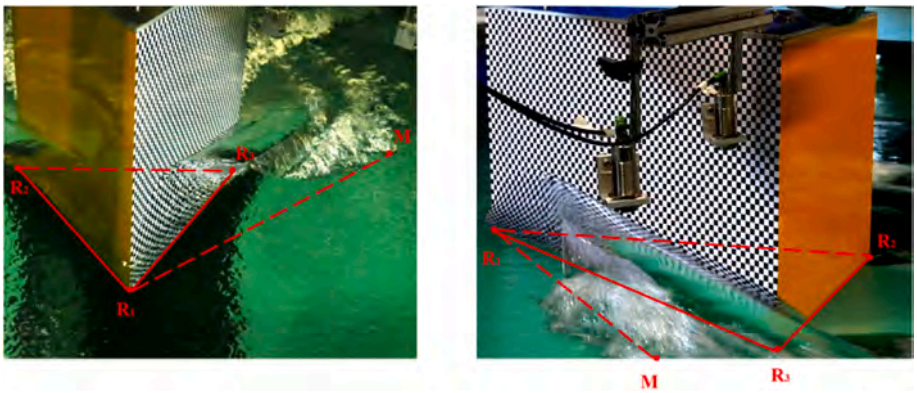

Fig. 16. Determination of experimental bow wave spreading angles.

Table 5
Comparison of experimental and numerical bow wave spreading angles.

Condition	CFD (°)	EFD (°)	Absolute Error (°)	Relative error (%)
$\theta = 15^{\circ}$	25.650	27.354	1.704	6.64
$\theta = 22.5^{\circ}$	41.050	39.542	−1.508	3.67
$\theta = 30^{\circ}$	53.600	55.752	2.162	4.01

section of secondary plunging in Top View and the mid-section of underwater air tubes in Bottom View, with all sections specifically adapted to each half-angle condition.

Fig. 19 demonstrates that increasing the half-angle leads to significantly larger bow wave heights and deeper submergence of air tubes. Analysis of z_{SD} shows that as the half angle increases, wave height fluctuations grow significantly faster than the mean wave height itself. This suggests that increasing the half angle significantly amplifies wave surface oscillations, leading to more occurrences of micro-scale bow wave breaking phenomena. The z_{SD} generated by submerged air tubes exhibit significantly greater intensity than surface phenomena. At increased half-angles (22.5° and 30°), quantitative measurements demonstrate the air tube-induced z_{SD} reach 1.8 times the magnitude of those produced by jetting and splashing.

4.3. Frequency characteristics

Although z_{SD} can characterize the intensity of fluctuations, a high z_{SD} does not necessarily correspond to high-frequency characteristics. Therefore, this study further investigates the effect of half angles on frequency characteristics of the bow wave height.

Several locations are selected for each condition to capture surface tearing and jetting. The normalized PSD of wave height fluctuations at these locations, with reference to their spatial positions are shown in Fig. 20. Points A_1, B_2, and B_3 are located at the first plunging break termination, exhibiting mesh-shaped wave surface fragmentation. The remaining points are correspond to jetting or splashing regions. The dashed line represents a power-law line with an exponent of $\alpha = -1.25$. Notably, in the high-frequency regime (above 30 Hz), the PSD for all conditions can be approximated by a power-law function of frequency, suggesting consistent turbulent energy cascading behavior:

$$E_{\eta}^{*}(f) \propto f^{-1.25} \tag{30}$$

Table 6 lists the real exponents at each selected point. The deviation is expressed as an average value with standard deviation: -1.25 ± 0.12, indicating a small spread of errors.

To further analyze the distribution of bow wave height energy across different frequency bands, two typical points are selected: one from the quasi-steady region and one from the strong breaking region. Their normalized PSD are shown in Fig. 21. At the quasi-steady point, the fundamental frequency band is mainly located between 0 and 10 Hz. Its

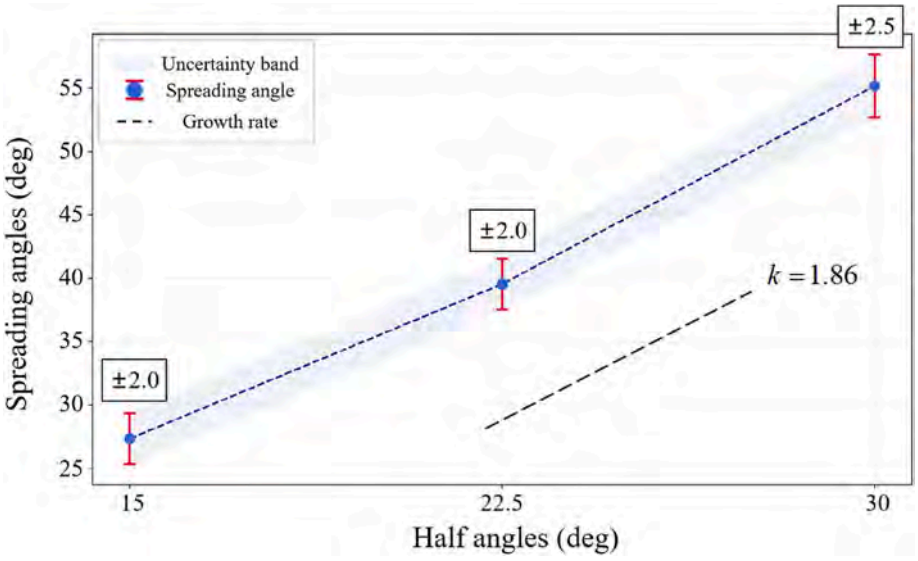

Fig. 17. Spreading angle-half angle phase diagram.

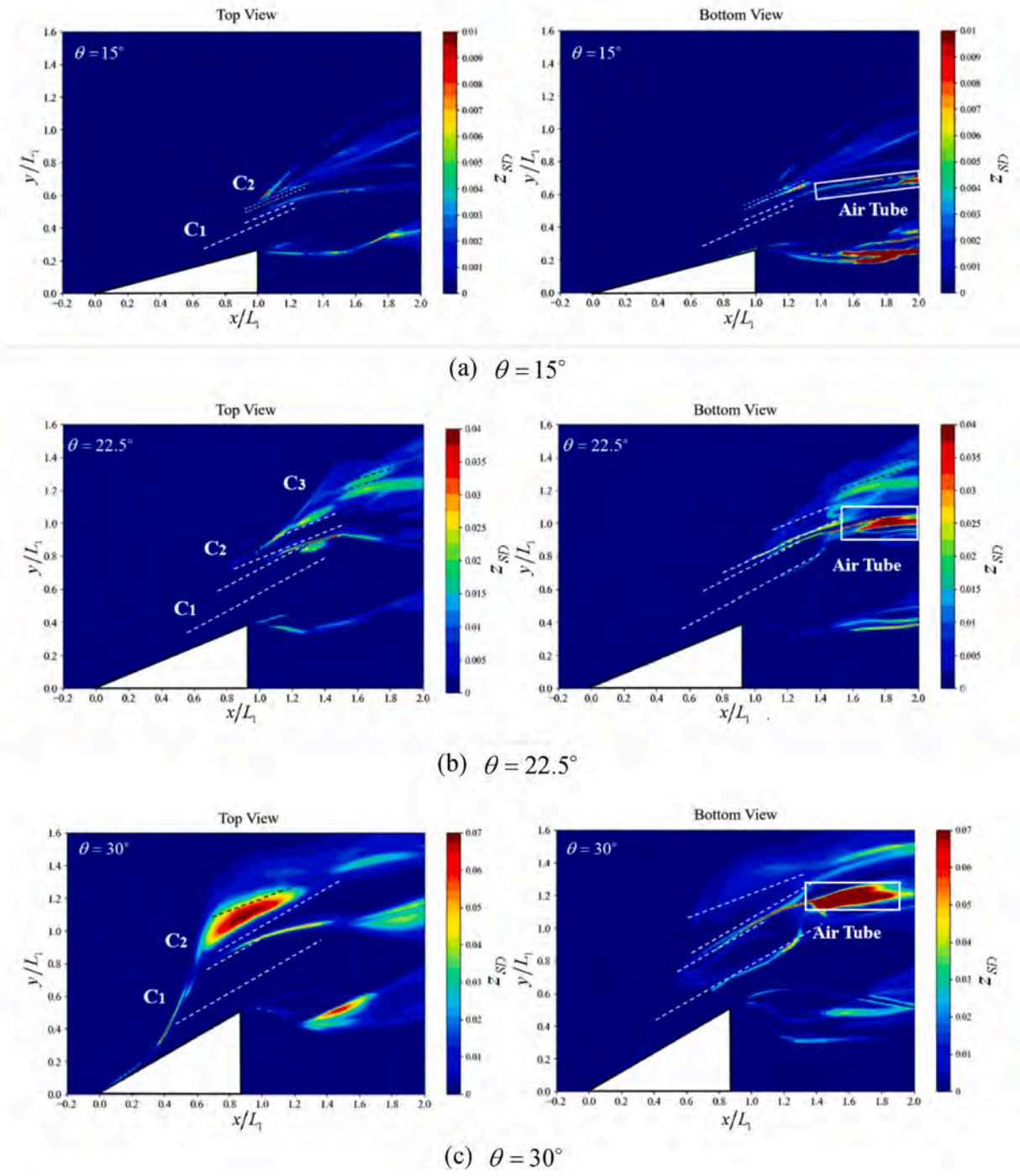

Fig. 18. Top and bottom views of z_{SD}

high-frequency oscillations are primarily observed in the 10–20 Hz range. At the strong wave breaking point, the fundamental energy is mainly distributed in the 10–20 Hz range. Its high-frequency oscillations appear primarily between 20 and 60 Hz. Therefore, the frequency spectrum of the bow wave generated by the wedge-shaped bow can be divided into four frequency bands: below 10 Hz, 10–20 Hz, 20–60 Hz, and 60–100 Hz.

Based on the established frequency band classification, σ_h is analyzed at different half angles. Using the $\theta = 30°$ condition as a representative case, Fig. 22 demonstrates the distinct σ_h distribution between Top and Bottom views within the <10 Hz range. Regions outside the bow wave area are masked, with the edges of each plunging event and the wake marked by dashed lines. Both views show that most of the energy in the quasi-steady regions is distributed <10 Hz with $\sigma_h \geq 90\%$. Accordingly, the critical frequency range associated with the quasi-steady region of bow wave breaking for the wedge-shaped bow is identified to be < 10 Hz. However, phenomena such as jetting, splashing, cavity, and underwater air tubes are shown to cause a significant increase in the high-frequency energy proportion, which in turn reduces $\sigma_h < 10$ Hz. The high-frequency energy is primarily observed in the second plunging region and outer spilling wave breaking area in the Top view, while in the Bottom view, it is mainly observed in the first and second plunging regions.

Therefore, to more clearly analyze the frequency characteristics of

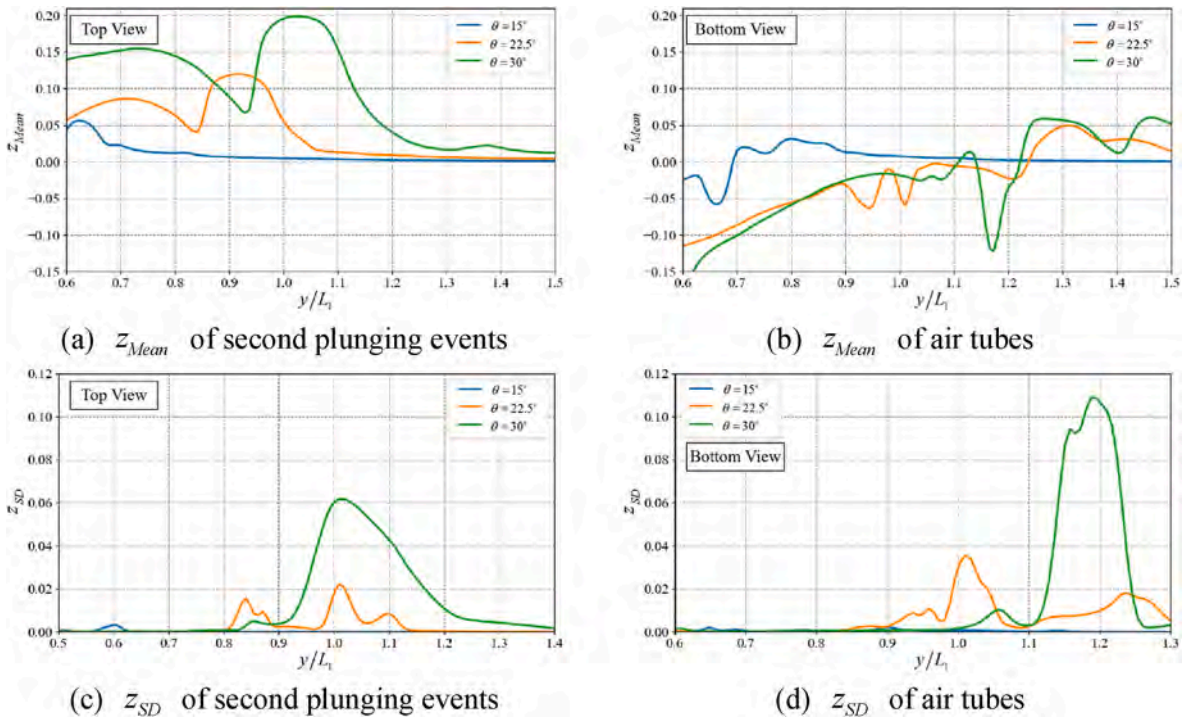

Fig. 19. Half angle effects on bow wave statistics.

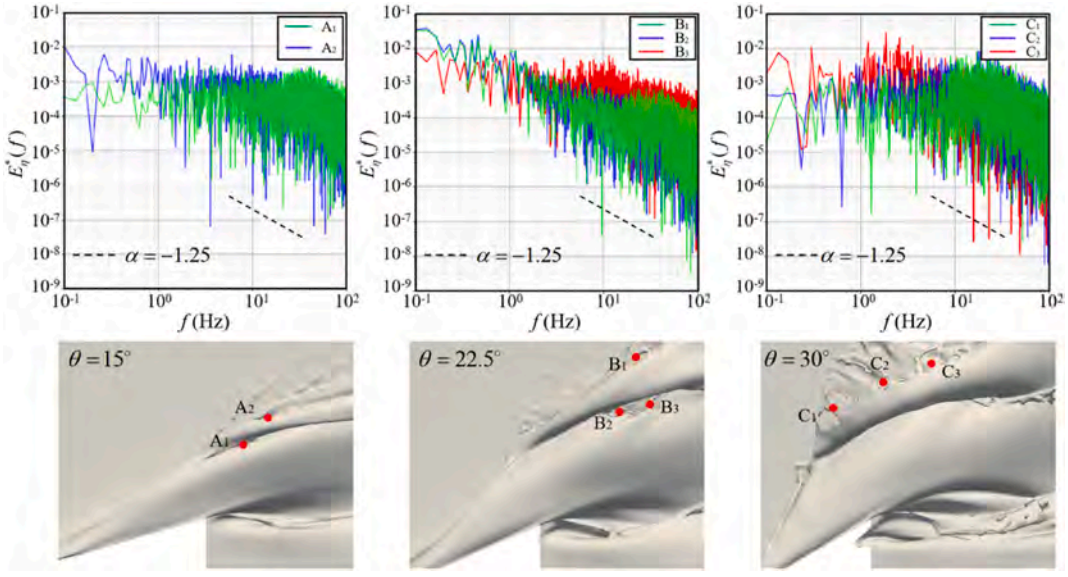

Fig. 20. Normalized PSD results at selected wave breaking locations.

Table 6
Normalized PSD power-law exponents at selected locations.

Points	A_1	A_2	B_1	B_2	B_3	C_1	C_2	C_3
Exponent	−1.161	−1.145	−1.460	−1.091	−1.223	−1.279	−1.289	−1.346

the bow wave breaking at different half angles, this study masks the non-primary regions from different views in order to focus on the key areas. Fig. 23 shows the σ_h distribution within each selected frequency range for the Top View. In the frequency range <10 Hz, as the half angle increases, the low σ_h region gradually expands and is primarily concentrated in the areas where jetting, splashing occur, as well as in the spilling wave breaking regions. As the half angle increases, the jetting and splashing, along with the more frequent disturbances between them and the free surface, introduce more high-frequency components into the bow wave. In the plunging wave breaking regions, the frequency characteristics of the bow wave show a clear pattern at different half angles. In the mid-frequency range (10, 20] Hz, the σ_h increases with the

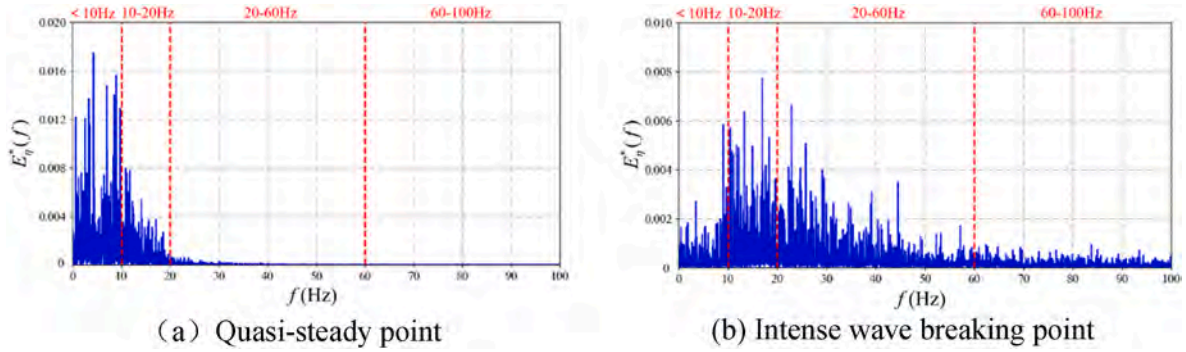

Fig. 21. Wave-height energy spectral distribution.

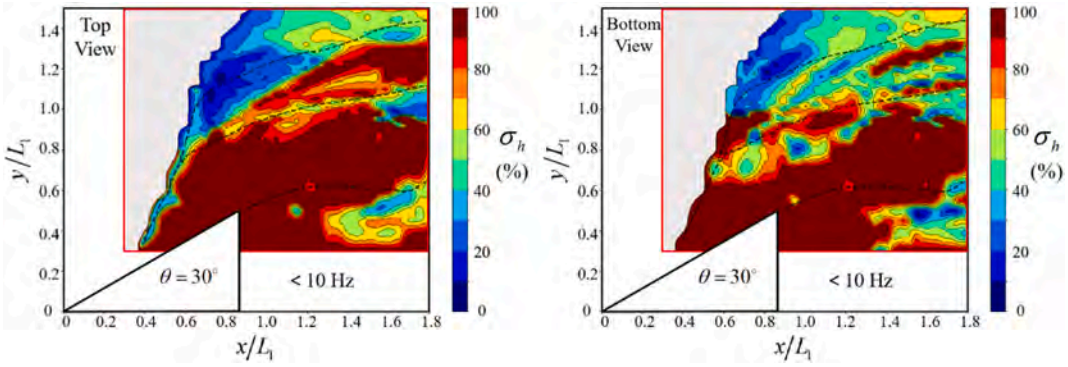

Fig. 22. Comparison of σ_h in top and bottom views.

half angle. The high-frequency range (20, 60] Hz is the critical frequency range for wave tearing, jetting, and splashing characteristics, where σ_h can reach 40 %–50 %, with some areas exceeding 50 %. For the extremely high-frequency range from (60, 100] Hz, in the jetting and splashing regions σ_h are still around 10 %–20 %. At $\theta = 15^\circ$ and $\theta = 22.5^\circ$,in the region where the mesh-shaped fragmentation occurs, σ_h is about 30 %. This is due to the very small distance between the jets in the surface tearing, which causes noticeable high-frequency fluctuations.

The spilling wave breaking regions also show the high-frequency features. Due to the differences in half angles, this characteristics vary significantly at different half angles. As the half angle increases, σ_h in the (10, 20] Hz mid-frequency range increases, while in the high-frequency ranges of (20, 60] Hz and (60, 100] Hz, σ_h decreases. This may be because a smaller half angle leads to more pronounced capillary wave phenomena in this region.

Fig. 24 shows the distribution within each selected frequency range from the Bottom perspective. As the half angle increases, the higher frequency components at the cavity significantly increase, and the oscillation frequencies of cavity shift toward the (10, 20] Hz range.

The air tube regions are highlighted with white frames. It can be seen that the (20, 60] Hz range remains the critical frequency band for the air tube characteristics, with σ_h exceeding 50 % in this range.

4.4. Energy distribution

The energy calculation utilizes measured bow wave lengths λ of 0.522 m, 0.693 m, and 0.823 m for $\theta = 15^\circ$, 22.5° and 30°, respectively. As shown in Fig. 25(a), cross-sections along the x-axis are selected to study the effect of the half angle on bow wave energy distribution.

Axial E_M^* distribution along selected x-axis cross-sections demonstrates a characteristic unimodal profile for all conditions, initially increasing due to energy transfer from the wedge-shaped bow to the surrounding water. Larger half angles result in more E_M^* transferred to the water. Then the bow wave breaking and turbulence leads to energy dissipation and a drop in E_M^*. The energy peak consistently occurs at the cross-section of first cavity formation. The peak values are 0.99×10^{-2}, 1.12×10^{-2}, and 1.56×10^{-2}, respectively, exhibiting a nonlinear increase. From the 15° case to the 30° case, the peak of the E_M^* increases by approximately 57.5 %. After that, E_M^* decreases rapidly with increasing distance. This may be due to both concentrated kinetic energy release and relatively stable potential energy. Notably, the energy decay slope steepens with increasing half angle, demonstrating more intense energy dissipation through enhanced wave breaking. The fitted decay slopes for the three conditions are -1.13×10^{-3}, -3.33×10^{-3}, and -5.20×10^{-3}, respectively. Moreover, at cross-sections progressively farther from the wedge, the axial E_M^* at $\theta = 15^\circ$ surpasses that of $\theta = 22.5^\circ$ and $\theta = 30^\circ$. This further indicates that more intense bow wave breaking leads to more pronounced energy decay.

Fig. 25 (b) presents the axial distributions of both potential and kinetic energy components. The axial E_K^* displays a characteristic bimodal distribution. At $\theta = 30^\circ$, the second peak demonstrates significantly stronger fluctuations, attributable to enhanced turbulence generation from the larger geometric disturbance. The second peak consistently occurs near the $x = 1.4\ L_1$ across all half angles. The local minimum between the two peaks results from energy dissipation during wave breaking processes. The second peak of E_K^* corresponds to the energy conversion from E_P^*. E_P^* begins to decay at $x = L_1$ across all half angles, as the downward plunging and acceleration of the water facilitate the conversion into E_K^*. The relatively low E_P^* at $\theta = 22.5^\circ$ may be attributed to the relative position of bow wave formation and wake effects.

Fig. 26 (a) presents the transverse energy distribution across selected y-axis cross-sections, revealing two characteristic peaks. The primary one aligned with the half-width of the wedge-shaped body and the secondary one linked to the second plunging wave crest. Due to the disturbance effect of the wedge-shaped body, E_M^* increases rapidly,

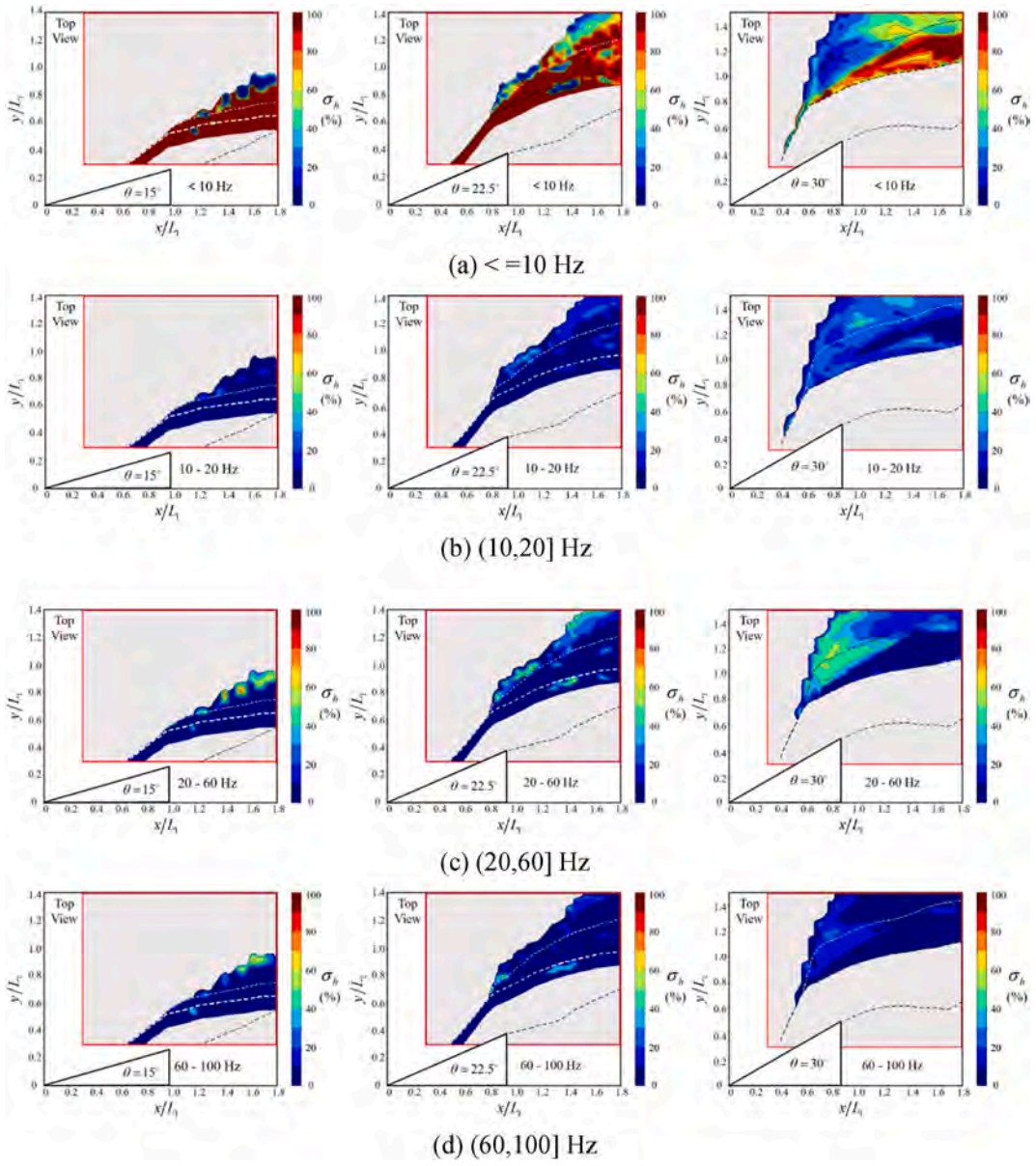

Fig. 23. σ_h across frequency ranges in the Top View.

forming the primary peak. As the distance away from the wedge-shaped bow, the transversal E_M^* decreases quickly. As the half angle decreases, the primary peak becomes more prominent. In contrast, the secondary peak grows substantially with increasing half-angle as the enhanced half angle promotes greater energy accumulation.

Fig. 26(b) presents the transverse distributions of both potential and kinetic energy components. Both the overall trends of E_K^* and E_P^* are similar to E_M^*. Since there is no direct conversion between kinetic energy and potential energy in the transversal direction, both show synchronized variation. Initially, E_K^* is almost the same at different half angles, but the initial E_P^* differs significantly and decreases as the half angle increases. This behavior stems from enhanced wake effects within the wedge's half-width region, which cause the initial peak of E_M^* to decrease with increasing half angle.

Finally, the proportion of kinetic energy σ_K is studied as Fig. 27. Along the axial direction, σ_K exhibits periodic fluctuations with consistent peak/valley positions across all half-angles, indicating similar energy evolution mechanisms despite geometric variations. Quantitatively, the mean σ_K increases with half-angle, measuring 50.8 %, 58.5 %, and 63.1 % for 15°, 22.5°, and 30° half angle respectively. The transverse distribution demonstrates less regularity, displaying an overall increasing trend with fluctuations. This behavior can be attributed to the fact that, upon the disappearance of the bow wave, the wave height recovers to its initial state prior to the disturbance velocity.

5. Conclusions

This study is based on PLIC and DDES numerical methods, simplifying the ship's bow structure to a wedge shape. The half angle is selected as a geometric factor to analyze its effect on bow wave breaking. Simulations of the bow wave breaking phenomena at different half angles are conducted, with half angles of 15°, 22.5°, and 30°, respectively. As the half angle increased, the bow wave breaking of the wedge-shaped structure significantly intensified. This study investigated the bow wave breaking phenomena based on flow field characteristics, bow wave height statistical features, bow wave height frequency characteristics, and energy distribution characteristics, and the following main conclusions are drawn.

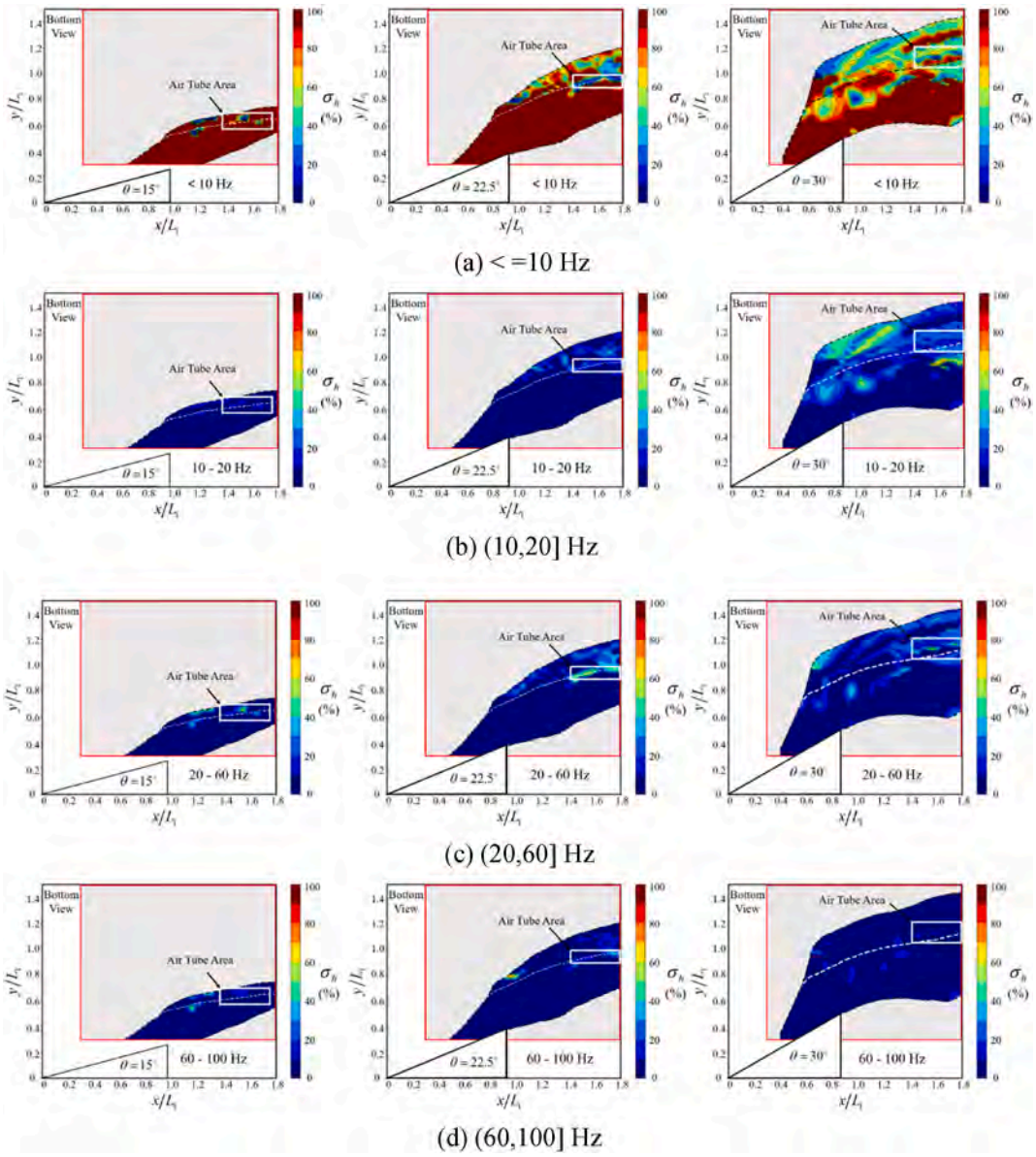

Fig. 24. σ_h across frequency ranges in the Bottom View.

(1) The study on velocity and vortex structures qualitatively explains the influence of the half angle on the bow wave breaking: (a) As the half angle increases, the axial velocity of the bow wave decreases, causing earlier plunging. The transversal and vertical velocities increase, resulting in a higher bow wave, enhanced air entrainment, and a greater tendency for secondary plunging wave breaking. (b) The vortex density and number of vortex pairs increase with the half angle, further intensifying wave breaking through interactions with the wave surface.

(2) The distribution and fluctuation intensity of the bow wave are analyzed from a statistical perspective: (a) The bow wave spreading angle induced by the wedge-shaped bow follows a pattern of 1.86 θ $\pm$2.5°. (b) As the half angle increases, the bow wave gains enough energy for a third unsteady plunging. But when it increase to a threshold (like 30°), strong dissipation prevents the third plunging. (c) With the increase of half angle, both the peak of z_{Mean} and the peak of z_{SD} increase, indicating more pronounced bow waves and more intense wave breaking. Oscillations of the bow wave primarily originate from jet, splashing, and submerged air tube. The z_{SD} of the air tube is greater than that of the jetting and splashing.

(3) The frequency characteristics of the bow wave breaking are analyzed using normalized PSD and Fourier modes: (a) The wave height PSD at high frequencies of regions such as surface tearing, jetting, and splashing follows a power-law decay with an exponent of -1.25 ± 0.12. (b) The critical frequency band for quasi-steady regions like initial plunging in bow wave breaking remains <10 Hz. (c) The frequency range of (20, 60] Hz is the critical frequency band for wave breaking structures such as jetting, splashing, and air tube, with σ_h about 40–50 %.

(4) From the perspective of energy distribution: (a) The energy distribution exhibits a strong correlation with wave-breaking phenomena. The axial E_M^* demonstrates a unimodal distribution, with its peak located at the first cavity formation. The transversal E_M^* displays a bimodal distribution, where the peaks correspond to the half-width of the wedge-shaped bow and the second plunging wave crest. (b) As the half angle increases, axial energy dissipation becomes stronger and the turbulence of E_K^* increases. (c) σ_K follows a similar axial distribution trend at different half angles,

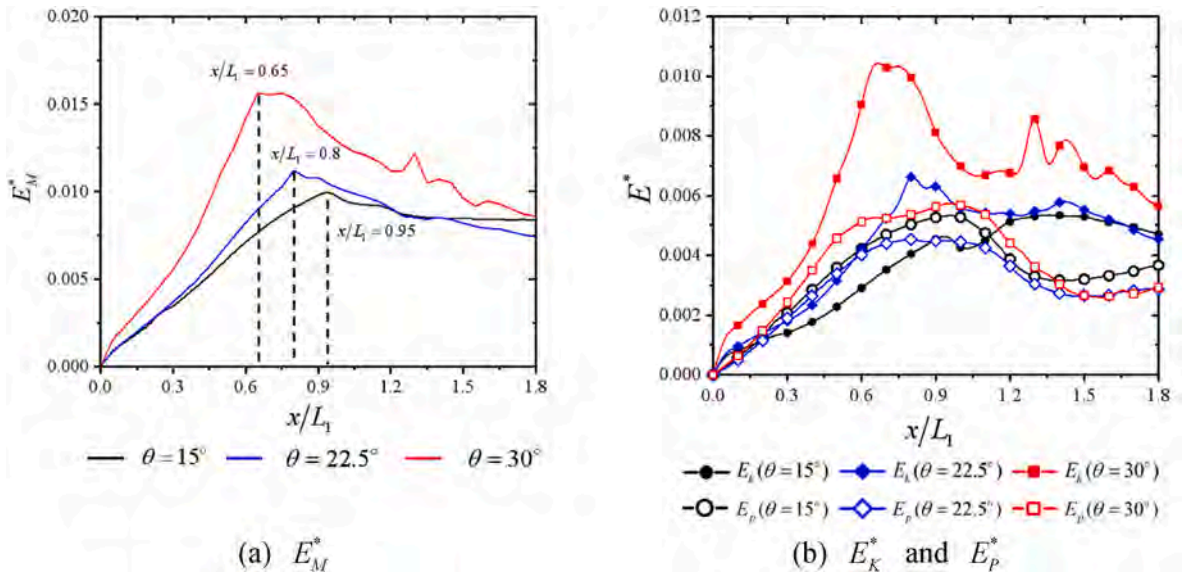

Fig. 25. Axial energy distributions.

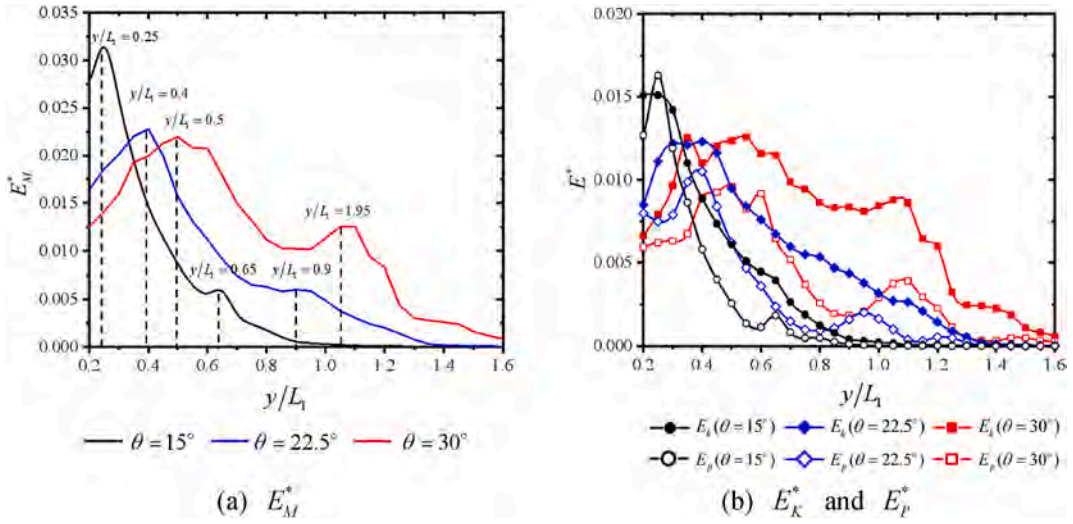

Fig. 26. Transversal energy distributions.

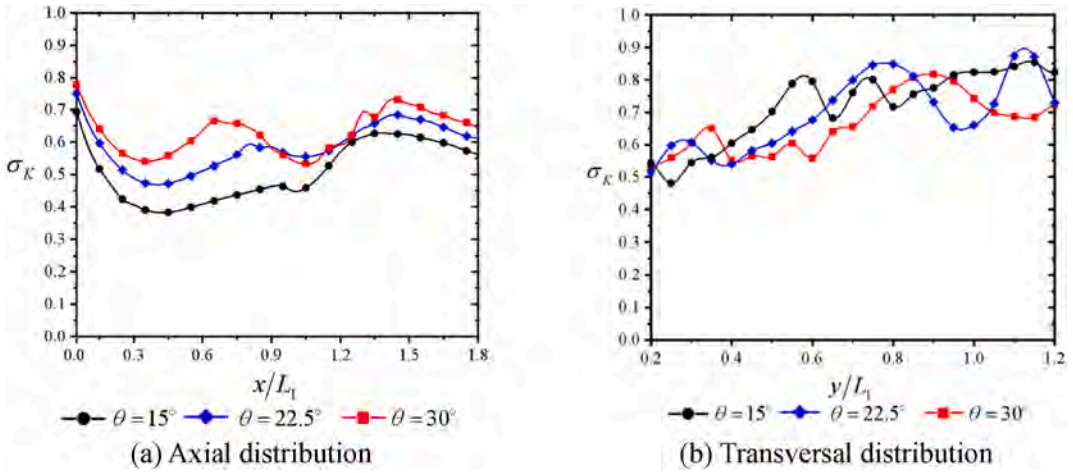

Fig. 27. Kinetic energy ratio distributions.

with the proportion increasing from 50.8 %, 58.5 %, to 63.1 % as the half angle increases from 15°, 22.5°–30°.

This study isolates the wedge half-angle as the sole geometric parameter to investigate its influence on bow wave breaking. However, this single parameter alone is insufficient to fully characterize or predict bow wave breaking behavior. Future work will extend the analysis to incorporate additional bow geometry factors.

CRediT authorship contribution statement

Xinyi Li: Writing – original draft, Visualization, Validation, Methodology, Investigation, Formal analysis, Data curation. **Bowei Song:** Resources, Project administration. **Jianhua Wang:** Writing – review & editing, Supervision, Software, Resources, Investigation, Funding acquisition, Conceptualization. **Decheng Wan:** Supervision, Software, Resources. **Jian Xu:** Supervision, Resources, Project administration.

Declaration of competing interest

The authors declare that they have no known competing financial interests or personal relationships that could have appeared to influence the work reported in this paper.

Acknowledgements

This work was supported by the National Natural Science Foundation of China (52471335 and 52131102).

References

Baba, E., 1969. A new component of viscous resistance of ships. J. Soc. Nav. Archit. Jpn. 125, 23–34.
Deike, L., Popinet, S., Melville, W.K., 2015. Capillary effects on wave breaking. J. Fluid Mech. 769, 541–569.
Delhommeau, G., Guilbaud, M., David, L., et al., 2009. Boundary between unsteady and overturning ship bow wave regimes. J. Fluid Mech. 620, 167–175.
Dong, R.R., Katz, J., Huang, T.T., 1997. On the structure of bow waves on a ship model. J. Fluid Mech. 346, 77–115.
Hu, Y., Liu, C., Hu, C., et al., 2021. Numerical investigation of flow structure and air entrainment of breaking bow wave generated by a rectangular plate. Phys. Fluids 33 (12).
Koo, B., Kang, Y.D., 2021. Numerical analysis on wave breaking around a wedge-shaped bow. J. Coast Res. 114 (SI), 559–563.
Li, X., Bao, F., Wang, J., et al., 2024. Spectral and statistical analysis of bow wave breaking characteristics of KCS ship. J. Hydrodyn. 36 (4), 593–608.
Liu, D., 2018. Experimental Study on Weak Three-Dimensional Wave Breaking [D]. Dalian University of Technology.
Liu, C., Gao, Y., Dong, X., et al., 2019. Third generation of vortex identification methods: Omega and Liutex/Rortex based systems. J. Hydrodyn. 31, 205–223.
Liu, W., Wang, W., Qiu, G., et al., 2022. KCS Unsteady bow wave breaking experiments for physics and CFD validation [C]. The 34th Symposium on Naval Hydrodynamics (SNH), Washington DC, USA.
Mao, T., Bao, F., Wang, J., et al., 2024. Numerical study of air cavity characteristics of bow wave breaking of KCS ship under different speeds. J. Hydrodyn. 36 (4), 678–692.
Menter, F.R., 1994. Two-equation eddy-viscosity turbulence models for engineering applications. AIAA J. 32 (8), 1598–1605.
Miyata, H., Inui, T., 1984. Nonlinear ship waves. Adv. Appl. Mech. 24, 215–288.
Noblesse, F., Delhommeau, G.E.R., Guilbaud, M., et al., 2008. Simple analytical relations for ship bow waves. J. Fluid Mech. 600, 105–132.
Olivieri, A., Pistani, F., Mascio, A.D., 2003. Breaking wave at the bow of a fast displacement ship model. Journal of marine science and technology 8, 68–75.
Olivieri, A., Pistani, F., Wilson, R., et al., 2007. Scars and vortices induced by ship bow and shoulder wave breaking. J. Fluid Eng. 129 (11), 1445–1459.
Ren, Z., Wang, J., Wan, D., 2018. Numerical simulations of ship bow and shoulder wave breaking in different advancing speeds [C]. The 37th International Conference on Ocean. Offshore and Arctic Engineering.
Roth, G.I., Mascenik, D.T., Katz, J., 1999. Measurements of the flow structure and turbulence within a ship bow wave. Phys. Fluids 11, 3512–3523.
Schwer, L.E., 2008. Is your mesh refined enough? Estimating discretization error using GCI. 7th LS-Dyna Anwenderforum 1 (1), 45–54.
Spalart, P.R., Deck, S., Shur, M.L., et al., 2006. A new version of detached-eddy simulation, resistant to ambiguous grid densities. Theor. Comput. Fluid Dynam. 20 (3), 181.
Strelets, M., 2001. Detached eddy simulation of massively separated flows. AIAA J. 1–18.
Sun, Z., Miao, X., Jagadeesh, C., 2020. Experimental investigation of the transonic shock-wave/boundary-layer interaction over a shock-generation bump. Phys. Fluids 32 (10).
Wang, Z., Yang, J., Stern, F., 2010. Numerical simulations of wave breakings around a wedge-shaped bow[C]. The 28th Symposium on Naval Hydrodynamics, Pasadena, California.
Wang, J., Ren, Z., Wan, D., 2020. Study of a container ship with breaking waves at high Froude number using URANS and DDES methods. J. Ship Res. 64 (4), 346–356.
Wang, J., Wang, W., Wan, D., 2023. Scale effects on bow wave breaking of KCS ship model: insights from DDES investigations. J. Hydrodyn. 35 (4), 668–678.
Wang, J., Shao, Y., Li, X., et al., 2025. Wave-breaking phenomena around a wedge-shaped bow. Phys. Fluids 37 (1).
Waniewski, T.A., 1999. Air Entrainment by Bow waves[M]. California Institute of Technology.
Waniewski, T.A., Brennen, C.E., Raichlen, F., 2001. Measurements of air entrainment by bow waves. J. Fluid Eng. 123 (1), 57–63.
Waniewski, T.A., Brennen, C.E., Raichlen, F., 2002. Bow wave dynamics. J. Ship Res. 46 (1), 1–15.
Xie, L., Wang, J., Wan, D., 2021. Study on the scale effect of bow wave breaking based on DDES. Shipbuilding of China 62 (2), 82–96.
Youngs, D.L., 1982. Time-dependent Multi-Material Flow with Large Fluid Distortion, Numerical Methods for Fluid Dynamics. Academic Press, New York.